

## Weak Field Population Control

### 4.1 Introduction

Coherent control remains a primary goal of ultrafast laser dynamics studies [1,2]. Research so far addresses several key categories, such as the use of resonant frequencies to control quantum wave packet interferences [2-5] and novel pulse shapes to control multi-order processes [2,6-10]. Optimization of coherent control has been achieved using various types of learning algorithms [8,11-13] [see previous chapter], but the nature of the mechanisms for the optimal results is not always readily apparent. This chapter will identify a class of pulse shapes that enhance the population transfer from a single state to multiple excited states, providing a basis for understanding the nature of optimal pulse shapes for both population transfer and quantum interferences in the superpositions. Pulse shapes that have been shown to enhance transient excited state population in a two level system will be applied to multiple excited states. All experiments will be analyzed using first order perturbation theory.

Much work has been devoted to the field of population transfer dynamics in the continuous wave regime [14], but only recently have well-established population transfer theoretical tools been applied to the wide bandwidth inherent to ultrafast spectroscopy [13,15-18]. For example, it has been shown that chirped pulses can be used to enhance population transfer dynamics in a multiphoton process [15,19] or even transiently in a single photon process [13,17]. It has been

shown that optimal enhancement of multiphoton dynamics can be achieved not by chirped pulses, but by applying constant phases to *blocks* of nonresonant frequencies relative to resonant frequencies [13,16,18], based on the  $t=0.0$  ps optimization described in the previous chapter. By using a frequency domain analysis, the optimal pulse shape is shown to depend primarily on frequencies that are near resonant, as will be discussed in detail in a later section.

This chapter considers the simultaneous control of both time dependent population transfer dynamics and superposition state quantum interferences using analytically optimal pulse shapes, in comparison to simple chirped pulse shapes and near transform-limited pulses. Of interest are the effects of resonant and nonresonant frequencies involved in the excitation of superposition states. By independently controlling not only quantum interferences between wave packet states, but also the population transfer dynamics to each state, the coherently controlled ionization yield at specific time delays is more than double that produced by a transform limited pulse in a two-state superposition pump-probe experiment. A two-color ultrafast laser experimental system, with pulse shaping, is used to isolate the coherent population transfer dynamics of a two-level superposition in  $\text{Li}_2$  molecules. The criteria for independent control of the coherent population transfer dynamics and quantum interferences are established. Extensions to more than two states are also discussed.

Simultaneous coherent control of two well-defined excited states unifies concepts concerning the dynamics between interfering superposition states and population transfer dynamics to individual states. As long as the interfering states

are sufficiently separated in energy from each other, the population transfer dynamics to each state can largely be independently controlled. Additionally, the relative phases of the multiple states are controlled during the process of population transfer. In the following sections, a theoretical framework for these experiments is first presented, followed by a summary of experimental considerations. Finally, experimental results are presented and discussed in the next section, along with a quantification of the limitations of enhancing photoionization using various pulse shapes. The degree to which the population transfer for two states can be independently controlled is quantified in that final section.

## 4.2 Theory

In the weak field limit, first-order time-dependent perturbation theory can be used to describe a single photon absorption. The excited state amplitude coefficient for a single state is described in the time domain [20]:

$$c_n(t) = \frac{\mu_{eg}}{i\eta} \int_{-\infty}^t \varepsilon(t') \exp(i\omega_{eg}t') dt', \quad (4.1)$$

where  $\mu_{eg}$  is the dipole moment matrix element between the excited and ground states,  $\varepsilon(t)$  is the electric field as a function of time, and  $\omega_{eg} = (E_e - E_g)/\eta$  is the transition frequency. Using similar logic to earlier work [16,18,21], this excited state amplitude can be approximated for positive time  $t$  by the frequency domain expression

$$c_n(t) = \frac{\mu_{eg}}{i\eta} \left\{ \tilde{\varepsilon}^*(\omega_{eg}) - \frac{i}{2\pi} \wp \int_{-\infty}^{\infty} \frac{\varepsilon(\omega) \exp[i(\Delta)t]}{\Delta} d\omega \right\}, \quad (4.2)$$

where  $\tilde{\varepsilon}^*(\omega_{eg})$  is the amplitude of the electric field at the transition frequency,  $\varepsilon(\omega)$  is the amplitude of light at frequency  $\omega$ ,  $\Delta = \omega - \omega_{eg}$  is the detuning, and  $\wp$  is the Cauchy principal value. The first term in Eq. (2) represents the resonant contribution to the excited state amplitude, and the second term represents nonresonant contributions. As  $t$  approaches infinity, the second term averages to zero, and Eq. (2) reduces to the resonant component; however the second term does not necessarily average to zero for small  $t$  (*i.e.*, within the pulse width). In the absence of any phase manipulation (*i.e.*, transform limited pulses), the nonresonant term will be greatly diminished for all  $t$ , since the  $\Delta$  term for  $\omega > \omega_{eg}$  is  $\pi$  out of phase relative to  $\omega < \omega_{eg}$  [18]. Additionally, the  $i/2\pi$  leading factor of the nonresonant term places the nonresonant contribution  $\pi/2$  out of phase with the resonant term. This phase relationship suggests that to bring all frequency components into phase at small  $t$ , an additional  $+\pi/2$  and  $-\pi/2$  phase must be added to the nonresonant frequencies above and below  $\omega_{eg}$ , respectively. Additionally, the  $1/\Delta$  dependence of the nonresonant term shows that the most influential frequencies will be those with the smallest detuning. These results may then be generalized to multiple excited states.

The  $1/\Delta$  dependence of the nonresonant wavelengths lends itself to the possibility that frequencies with a large  $\Delta$  can be manipulated with minimal influence on the excited state coefficient dynamics. This will allow for the manipulation of multiple states, provided that the energy separation between

states,  $\Delta\omega$ , is great enough that all frequencies near one state have little effect on any other states. For a two-state superposition, a lower limit of the degree to which the population transfer to state  $i$  can be independently controlled,  $I_{PTi}$ , is quantified as

$$I_{PTi} = 1 - 2n \left| \int_{\Delta\omega/2}^{\pm\infty} d\Delta' \varepsilon(\Delta_i')/\Delta_i' \right|^2, \quad (4.3)$$

where  $\Delta\omega$  is the difference in energy between the superposition states ( $\Delta\omega=\omega_i-\omega_j$ ), the second limit of integration ( $\pm\infty$ ) has the same sign as  $\Delta\omega$ , and  $\varepsilon(\Delta')$  is the amplitude of the electric field at a specific detuning. The factor of 2 accounts for destructive interference, and  $n$  normalizes the expression so that the second term reaches a maximum of 1. Physically speaking,  $I_{PTi}$  is a measure of the cumulative intensity of all nonresonant contributions to a particular population at a specific time relative to the ideal case (*i.e.*, single control channel). In the case where two states have degenerate energies (*i.e.*,  $\Delta\omega=0$ ) with a uniform energy spectrum,  $I_{PT}=0$ , the states can not be independently controlled. On the other hand, in the limit of  $\Delta\omega=\pm\infty$ , the second term goes to zero, and the states are completely independent of each other. This analysis assumes a regime where the spectrum is divided into an arbitrary number of “control channels,” with a specified bandwidth devoted to the control of each state. The spectrum is divided into two or more regions, and the integrated value of  $\varepsilon(\Delta_i')/\Delta_i'$  inside the control channel for state  $i$  is compared to  $\varepsilon(\Delta_i')/\Delta_i'$  outside of its control channel. Increasing the number of states involved in a control scheme will likely decrease the spectral width of the control channel for any state, decreasing the degree to

which that state can be independently controlled. In the discussion below, we use “control channel” to refer to large blocks of wavelengths surrounding each resonant transition and “resonant control channel” or “resonance” to refer to very small bandwidth regions centered on each resonant transition.

Lithium dimer ( $\text{Li}_2$ ) is used as a model system to investigate the extent to which nonresonant frequencies can be used to control multiple excited state coefficients with a single pulse. The relevant potential energy curves in  $\text{Li}_2$  are shown in Fig. 2.1 [22-24]. From a single launch state, two rovibrational states ( $v_E=9, J_E=27$  &  $29$ ) are accessible within the bandwidth of the pump laser, creating a time-dependent wave packet. A probe pulse ionizes the coherent superposition at various pump-probe time delays to obtain the signal. For parallel pump and probe polarizations (referred to as “parallel probe”), the presence of multiple rotational states in the wave packet produces a coherent superposition state with oscillations at a frequency equal to the energy difference between the states [25] [see Fig. 4.1]:

$$S(t) \equiv |pr_1|^2 |c_1(t)|^2 + |pr_2|^2 |c_2(t)|^2 + 2|pr_1 pr_2| |c_1(t)c_2(t)| \cos[\Delta\omega t + \Delta\phi(t)] \quad (4.4a)$$

where  $pr_1$  and  $pr_2$  are constants related to the probe step (not discussed here); the energy separation,  $\Delta\omega$ , is  $42 \text{ cm}^{-1}$  ( $1.5 \text{ THz}$ ); and  $\Delta\phi$  is the relative phase between the wave packet states at time  $t$ . In contrast, for a probe polarization oriented at the magic angle ( $\sim 55^\circ$ ) with respect to the pump polarization (“magic-angle probe”), the coherent oscillation is completely suppressed, so

$$S(t) = |pr_1|^2 |c_1(t)|^2 + |pr_2|^2 |c_2(t)|^2. \quad (4.4b)$$

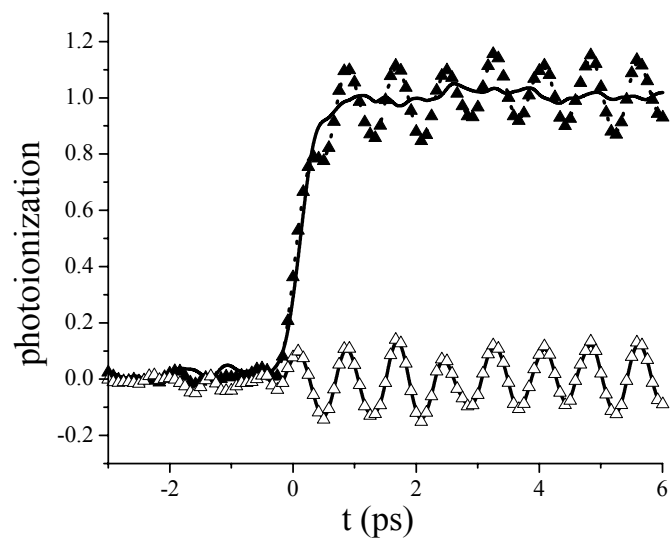


Figure 4.1: Pump-probe traces at parallel (▲) and magic angle (solid line) pump-probe polarizations, along with the difference ( $\triangle$ ) between the traces for unshaped pump pulses. These traces correspond to the total, incoherent, and coherence portions of the signal, respectively, with the raw signals normalized to an average value of 1.

This suppression is possible because the coherent oscillation is rotational in nature.[6,24] Hence, by manipulating the probe polarization, we can select whether the signal reflects a full wave packet trace or simply the ground to excited state population transfer dynamics. Furthermore, by subtracting the magic-angle probe signal from the parallel probe signal, we are left with just the coherent oscillation piece

$$S(t) = 2|pr_1pr_2||c_1(t)c_2(t)|\cos(\Delta\omega t + \Delta\phi). \quad (4.4c)$$

The probe step consists of an ultrafast pulse of a different color than the pump pulse [26]. This aspect of the signal was not considered above for simplicity. The color of the probe pulse is chosen so that the probability for a probe-pump (*i.e.*,  $t < 0$ ) ionization pathway is below the noise level, allowing time dependent ionization to occur only at positive time delays. There is a constant background component to the photoionization signal at all time delays, and this has also been subtracted out of the signals. Hence, the observed photoionization signal only shows the time dependent coefficient buildup behavior and the quantum interference of the superposition state as described in Eq. (4.4).

### 4.3 Experiment

The lithium sample is contained in a heat pipe at 1050 K and is photoionized by a three step excitation process. An overview of the laser system is given below, but details can be found in previous work [13,26], and in chapter 2. In this experiment, a narrow bandwidth continuous wave (cw) laser, an ultrafast amplifier system, and an optical parametric amplifier (OPA) are used, and all but the OPA are pumped by a 27 W argon ion laser. The frequency of the

cw laser is tuned to a specific  $A^1\Sigma_u^+ \leftarrow X^1\Sigma_g^+$  resonance (606.954 nm) of  $Li_2$ , producing a pure launch state ( $v_A=11, J_A=28$ ) on the first excited electronic state. The ultrafast regenerative amplifier is seeded by a 76 MHz oscillator to produce 180 fs [full width half maximum (FWHM)] ultrafast pulses at a 200 kHz repetition rate, near the 800 nm central wavelength with 8 nm (FWHM) bandwidth. These ultrafast pulses are split into two beams, with 25% of the light becoming the pump pulse and 75% of the light frequency doubled to pump the OPA. The resulting 15 mW OPA output is a train of nearly transform limited pulses with a 200 fs FWHM pulsewidth and a central wavelength of 640 nm. The OPA output is variably time-delayed relative to the pump pulse via a precision delay stage. This OPA wavelength is used since in the pump-probe regime, it yields a strong photoionization while producing very little photoionization in the probe-pump regime [see Fig. 2.1].

To shape the pump pulse, it is sent through a dispersion free pulse shaper [27,28]. In the pulse shaper's Fourier plane, a liquid crystal spatial light modulator (SLM) is used to shape the spatially dispersed pump light by independently attenuating and/or applying phase to 128 individual frequency components (SLM pixels) of the pump light. The central frequencies imaged onto the SLM pixels are separated by approximately  $4 \text{ cm}^{-1}$  with a single frequency spot size of approximately 1.7 pixels. Normally, the 8 nm FWHM pulses are imaged onto the SLM to achieve a bandwidth of 40 pixels FWHM. Pixellation and finite spot size effects limit the temporal pulse shaping to be within a window of about  $\pm 4 \text{ ps}$  around time zero.

The cw laser, pump, and probe pulses intersect in the interaction region in the center of the heat pipe. The ions are produced between two parallel plates separated by 1 cm with a 10 V potential applied across the interaction region. The cw light is optically chopped, and the resulting current is detected with a lock-in amplifier that is synchronized to the cw modulation.

To study the effects of nonresonant frequencies, two classes of pulse shapes have been used to enhance transient photoionization effects, shown in Fig. 4.2. The first class, which has previously been studied in the context of a single resonance [17] (“chirp-type spectrum”), has a quadratic phase applied across the frequency spectrum around each resonance with the form  $\phi(\omega)=c\Delta^2 + \phi_k$ , where  $\Delta=\omega_i-\omega$  is the detuning from the nearest resonance, and  $\phi_k$  is a constant phase [see Fig. 4.2a]. The constant phase,  $\phi_k$ , is applied to the entirety of one of the control channels to control the phase of the wave packet interferences. Here, the time delay is adjusted by varying the magnitude,  $c$ , of the quadratic phase. An optimal phase mask for population transfer comprises the second class, called the “phase-jump spectrum”; this phase mask involves the application of  $\pi/2$  and  $-\pi/2$  radians above and below resonance, as established in several recent works [see Fig. 4.2b] [13,18]. The resonant portion of the control channel is defined here as a block of two pixels ( $\sim 8 \text{ cm}^{-1}$  FWHM) centered on a specific transition, chosen to avoid attenuating the long time delay signal by diffraction [13]. So, in effect, “resonance” actually refers to the smallest practical bandwidth achievable by our pulse shaper around each transition. To vary the timing of the optimal photoionization, a linear phase versus wavelength is added to the nonresonant

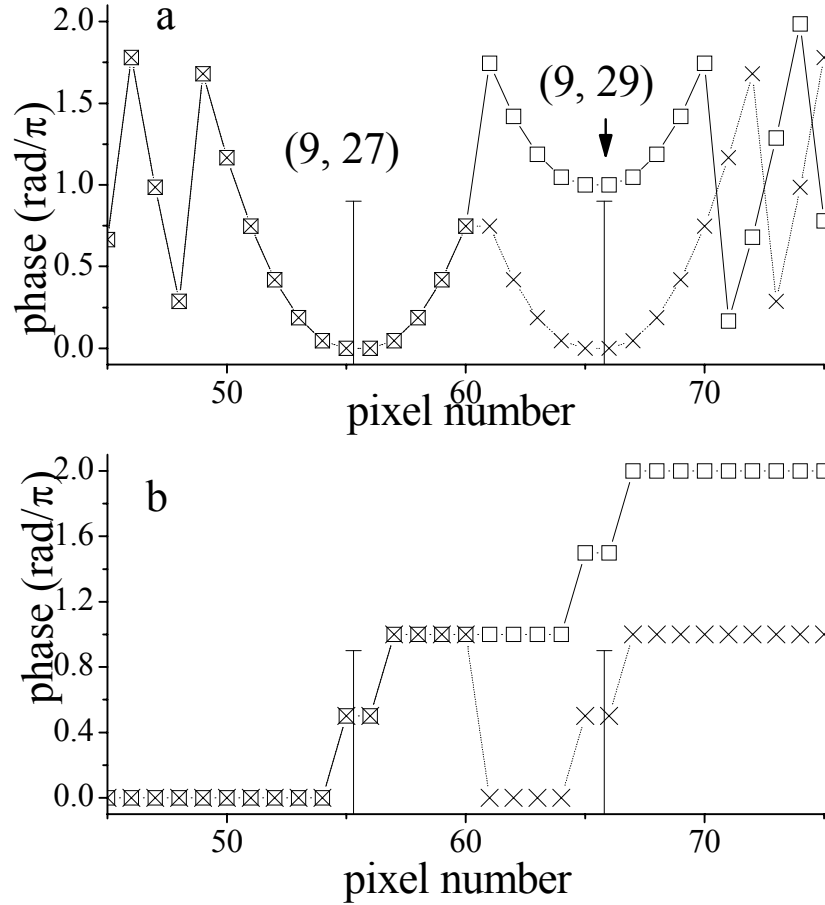


Figure 4.2. Phase mask classes used in this chapter. In both panels, quantum state resonances ( $v_E=9$ ,  $J_E=27$  &  $29$ ) are marked with vertical lines. Relative phase offset of  $0.0$  and  $\pi$  radians between control channels are represented by crosses (X) and squares ( $\square$ ), respectively. Panel a: Chirp-type spectra. The degree of quadratic phase,  $c$ , is defined by  $\phi(\text{pixel}) = c \times (\Delta_{\text{pixel}})^2$  where  $\Delta_{\text{pixel}}$  is the separation in pixels from the nearest resonance. Panel b: Phase-jump spectra. A phase of  $+\pi/2$  and  $-\pi/2$  is added to the frequencies above and below resonance, respectively. A linear phase of  $\phi(\text{pixel}) = c \times \Delta_{\text{pixel}}$  is added to the phase masks to induce a time shift in the population transfer (not shown). The phase on pixel 56 is always the same as that on pixel 55, and the phase on pixel 66 is always the same as that on pixel 65.

portion of the phase-jump phase profile. As in the case of the chirp-type spectrum, the relative phase of the wave packet states using the phase-jump spectrum is manipulated by adding a constant phase to only one of the control channels.

#### **4.4 Results and Discussion**

This section will first analyze the ability to control quantum beats while applying a previously studied chirp-type phase mask around each state, but extended to a quantum superposition. Next it will be shown that the phase jump spectrum gives a much greater enhancement in the transient photoionization. It will further be shown that the timing of the peak photoionization for the phase jump spectrum can be much more precisely controlled than the chirp-type spectrum. Finally, the nonresonant contributions to the photoionization will be compared to a simple model to quantify the degree to which the quantum states in the superposition can be independently controlled.

To demonstrate the separability of the population transfer dynamics from the wave packet oscillations, we first examine the previously studied case of the chirp-type spectrum, with results for the two states at the magic angle [Eq. 4.4b] and parallel probe minus the magic angle [Eq. (4.4c)], shown in Fig. 4.3[49]. The population transfer dynamics in the upper part of the figure show several traits of the buildup produced by a strictly chirped pulse. After time zero, there is a peak in the excited state population followed by a short period of ringing. After just a few picoseconds, this ringing decays, leaving a constant value for the



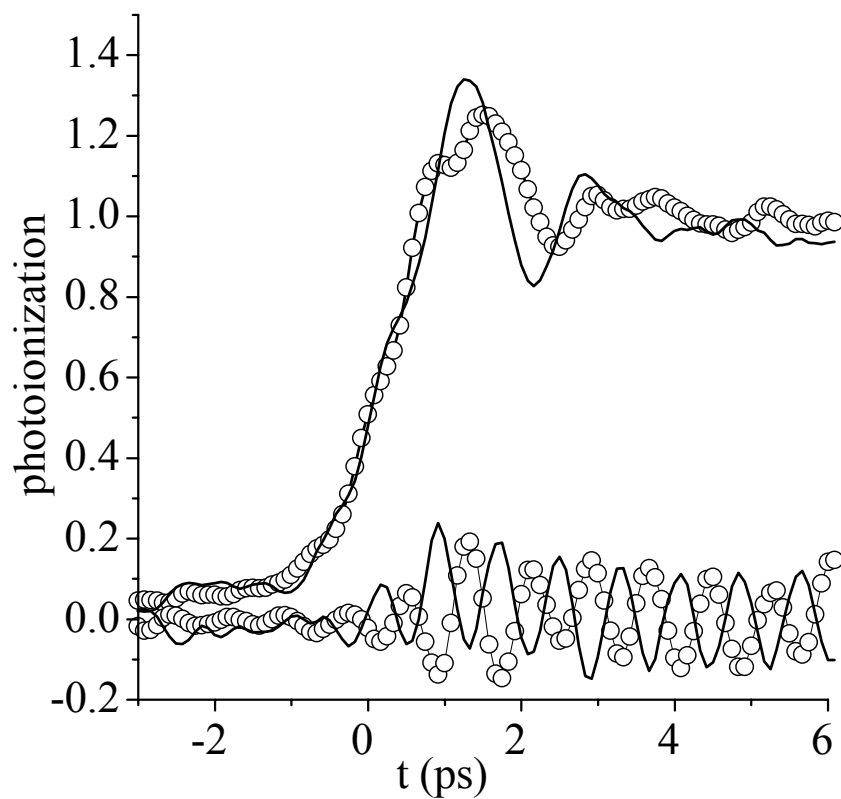


Figure 4.3. Chirp-type pump spectrum transients. The upper solid line and circles (○) represent the magic-angle probe transient for  $\pi$  and 0 radians relative phase between control channels, respectively, and a chirp factor of 0.2. The lower solid line and circles (○) represent just the coherent oscillations produced with the same phase masks as above.

excited state population. Notice that these traits are present for both zero and  $\pi$  relative phase between the control channels, and in both cases there is a peak in the excited state population around a planned delay time of 1.2-1.3 ps, depending on the degree of chirp, in this case 0.2 chirp factor. The coherent oscillations, which are simply the difference between the parallel and magic-angle probes, are also predictably controlled. Clearly, a  $\pi$  phase shift of one coherent oscillation relative to the other can be induced, which is simply a result of adding  $\pi$  phase to only one of the resonant control channels.

Additionally, around 1.2 ps, the amplitude of the coherent oscillations passes through a maximum, as expected from Eq. (4.4a). The combination of the population transfer dynamics and the wave packet interferences produces a clear peak in the photoionization signal at 1.2 ps despite the slightly decreased population transfer using zero phase offset between control channels.

The analysis of the chirp-type spectrum above establishes that both the population transfer dynamics and wave packet interferences can be independently controlled. This section now explores more optimal phase masks to maximize the photoionization due to the population transfer dynamics in conjunction with the interference of two states at specific short pump-probe time delays.

Several magic angle and parallel pump-probe data are summarized in Fig. 4.4. A pump-probe transient obtained with the phase-jump spectrum of Fig. 4.4 clearly shows an enhancement in the excited state population, in addition to the proper phasing of the coherent oscillation at  $t=0$ , shown in Fig. 4.4a. In these signals, the background signal has been subtracted out, and the remaining

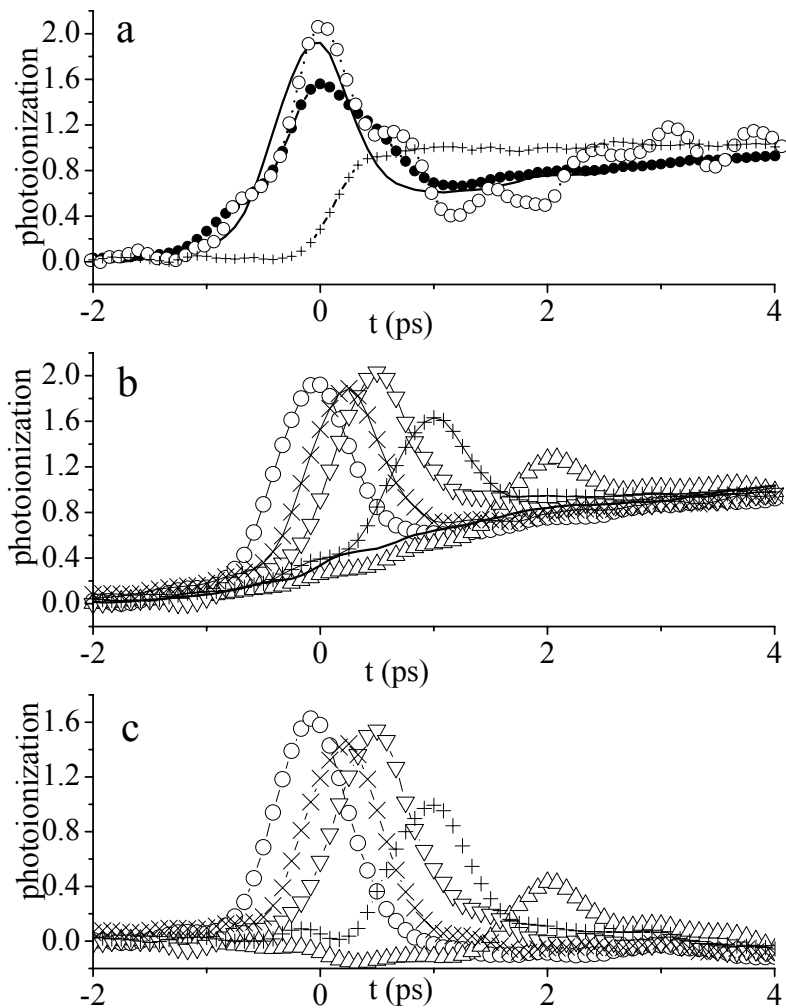


Figure 4.4. Phase-jump pump spectrum transients. Panel a: Magic angle probe traces produced using zero phase offset (●) and  $\pi$  phase offset (solid line) between the control channels, and parallel probe photoionization signal (○) for zero control channel phase offset. A trace produced by an unshaped pump pulse with magic angle probe (+) is included for reference. Panel b: Population transfer traces adding varying degrees of linear phase to nonresonant frequencies with  $\pi$  phase offset between wave packet resonances. The nonresonant contributions were timeshifted to have peak photoionization occur at 0.0, 0.25, 0.5, 1.0, and 2.0 ps (○, ×, ▽, +, and △, respectively). The solid line represents an attempt to shift the nonresonant contribution to a time beyond the capabilities of the experimental apparatus, resulting in a purely resonant excitation effect. Panel c: Nonresonant effects on the population transfer at various time delays. Traces were generated by subtracting the purely resonant contribution of the population transfer trace from the total population transfer signal (same symbols as in panel b). photoionization signal has been normalized to the signal at  $t=\infty$ , which has been shown to

depend only on resonant wavelengths and hence is constant in these studies[25]. Two

population transfer traces (magic-angle probe) are shown, along with a total wave packet signal (parallel probe) that is designed to have a maximum in the quantum beat at the same delay (0.0 ps) as the maximum in the population transfer. The population transfer traces use phase masks with 0 and  $\pi$  relative phase between two control channels, and the full wave packet signal is set to have 0 relative phase between the two control channels [the X's in Fig. 4.2b]. Both population transfer traces show a peak at the same pump-probe time delay, with the case of  $\pi$  relative phase between control channels [the  $\square$ 's in Fig. 4.2b] having the larger peak amplitude.

Of all relative phases between control channels of the phase-jump class, the case of zero relative phase is the least optimal for population transfer. This is so because all of the wavelengths between the two wave packet states in one control channel maximally destructively interfere with the buildup of the other control channel. For example, the light on pixels 57-60 maximally and destructively interferes with the buildup of state (9,29), where the control channel includes pixels 61-128. Even so, the wave packet interference produces a global maximum in the photoionization at 0.0 ps pump-probe delay. A net gain in the photoionization relative to a non-interfering condition can always be achieved as long as the wave packet interference amplitude exceeds one minus the degree of independent control, or when  $|pr_1pr_2||c_1(t)c_2(t)| > 1 - I_{PTi}$  from Eqs. (4.3) and (4.4). Note that for a multiple state superposition,  $1 - I_{PTi}$  increases, but simultaneously multiple coherent oscillations can constructively interfere, counteracting the decrease in degree of independent control inherent to the smaller control channel sizes of a multiple state system.

In Fig. 4.4b several population transfer traces are shown for the phase jump spectra with varying amounts of linear phase added just to the nonresonant frequencies; these traces are generated using only  $\pi$  relative phase between the wave packet resonances. The peak height and time for each trace is noted and will be discussed later. Evident in this figure is that for each trace there is a slow, monotonic buildup ( $>4$  ps) of population attributable to resonant (and very near resonant) frequencies coupled with a much shorter timescale population transfer attributable to nonresonant frequencies. By subtracting the resonant portion of the traces from the full traces, purely nonresonant effects can be analyzed [see Fig. 4.4c]. The time-shifted nonresonant contributions to the population transfer show peak widths between 750 fs and 790 fs FWHM. This data will be used later to quantify the degree to which the superposition states can be independently controlled.

The phase-jump spectrum permits a higher degree of coherent control than the chirp-type spectrum by obtaining a greater enhancement in the population transfer and by allowing more precise timing of the peak of the photoionization signal [see Fig. 4.5]. Figure 4.5a shows the peak excited state populations as a function of time for the two pulse shape classes. At short times, the phase-jump spectrum doubles the excited state population, whereas the chirp-type spectrum shows a maximum of 30 percent improvement of the photoionization signal. The

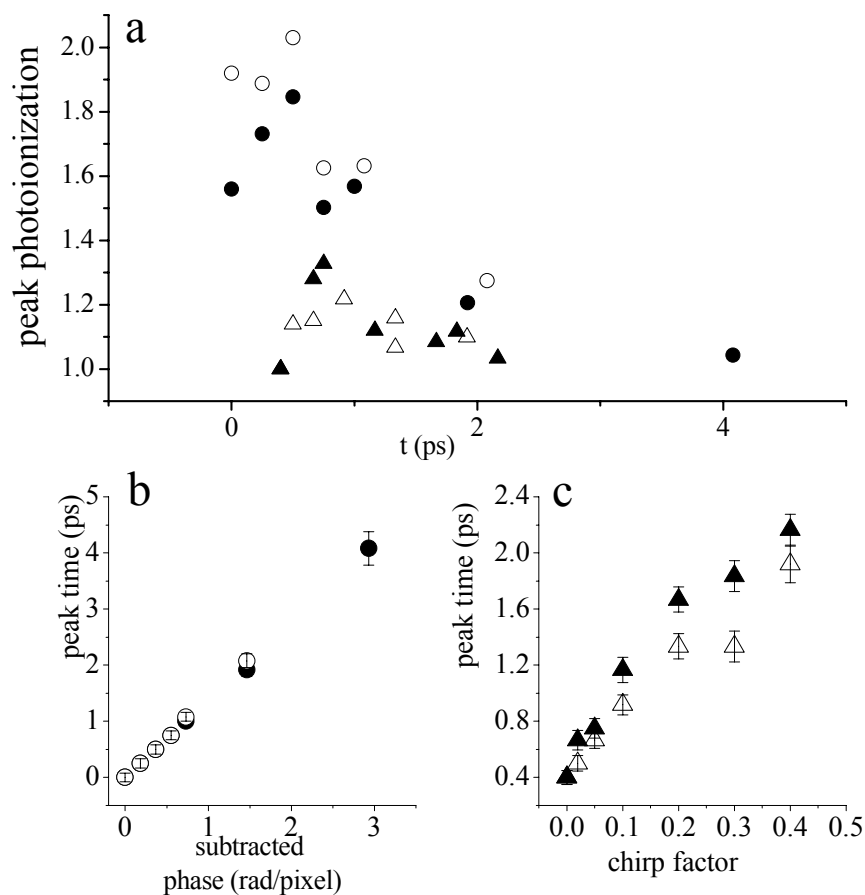


Fig. 4.5. Comparison of control capabilities using the phase-jump spectrum versus the chirp-type spectrum. In all panels, peak photoionization was monitored for various degrees of chirp type pulse shapes (triangles) and time shifted phase jump pulse shapes (circles). Filled symbols denote 0 relative phase between control channels, and open symbols represent  $\pi$  relative phase. Panel a: Peak photoionization comparison as a function of designed peak time delay. Data is collected by analyzing peak heights as shown in Fig. 4.4b, for example. The peak photoionization for the unshaped spectrum (*i.e.*, degree of chirp = 0) is represented by the chirp type spectrum data point at 0.4 ps and is normalized to 1. Panel b: Peak times as a function of degree of linear phase added to the standard phase-jump spectrum. Panel c: Peak times as a function of the degree of quadratic phase applied around each resonance for the chirp-type spectrum.

phase-jump spectrum shows greater population transfer enhancement than the chirp-type spectrum because the phase-jump shape assures that all non-resonant contributions come into phase simultaneously. This is in contrast to the chirp-type situation, in which only certain nonresonant contributions are in phase at any one time. For the phase jump spectrum, the timing of the peak of the photoionization signal can be controlled precisely, as shown in Fig. 4.5b. Note that in this regime the time delays of the peak photoionization signals are chosen by time-shifting the nonresonant contributions to the population transfer by simply adding a linear phase to the basic phase-jump pattern, based on the relation  $\Delta t = d\phi/d\omega$ . Relative to the phase-jump spectrum, the timing of the peak population transfer in the chirp type spectrum is not controlled as successfully. Notice in Fig. 4.5c that the peak timing follows a roughly linear relationship with the degree of chirp, but the deviation from a linear relationship is substantial. This can partially be attributed to wrap-around effects (*i.e.* the phase can only be defined modulo  $2\pi$ ) and “overlap” between the separate shaping channels of the phase mask. For example, the truly quadratic phase for the control channel around state  $(v_E, J_E)=(9,27)$  is defined to stop at pixel number 60, but with chirp factor  $c=0.2$  and  $\pi$  relative phase between wave packet states [see Fig. 4.2b], pixel 61 fits well onto the quadratic progression. This in essence extends the size of the control channels. While this will be true for some chirp factors, it will not be true for others, accounting for the scatter in Fig. 4.5c.

The mechanism for the increase in population transfer for the phase jump spectrum can be attributed to off resonant Rabi oscillations. In the weak field limit, the

Rabi frequency  $\Omega(\Delta) = \left\{ \Delta^2 + \left[ \mu_{eg} \epsilon(\Delta + \omega_{eg}) / \eta \right]^2 \right\}^{1/2}$  reduces to  $\Omega(\Delta)=\Delta$ , since

$[\mu_{eg}\varepsilon(\Delta + \omega_{eg})]^2 \ll \Delta^2$  for values of  $\Delta$  with non-negligible electric field amplitudes [14].

Additionally, given that the amplitude of any nonresonant oscillation is proportional to  $\varepsilon(\Delta + \omega_{eg})/\Delta$  [29], the total of all nonresonant contributions to the excited state populations can then be formulated as  $c(t) \propto \int_{-\infty}^{\infty} d\Delta \left[ \varepsilon(\Delta + \omega_{eg})/\Delta \right]^2 \sin^2(\Delta t/2 + \phi(\Delta))$ . Notice the similarity of this representation to Eq. (4.2). To bring all of these sine waves into phase at  $t=0$ , a phase mask with  $+\pi/2$  and  $-\pi/2$  radians applied to the positive and negative detuned wavelengths, respectively, must be implemented. At the resonant wavelength (*i.e.*, where  $\Delta=0$ ), the optimal phase will be intermediate between the positive and negative detuning, or zero degrees. Thus we have the same optimal phase pattern as predicted by Eq. (4.2). In contrast, for the chirped phase pattern, not all nonresonant Rabi oscillations come into phase simultaneously. Rather, there is a series of partial recurrences in time; this is observed as a ringing in the signal.

To quantify the degree to which the two states in the experiments described here can be independently manipulated, a model based upon Eqs. (4.1) and (4.2) is implemented. This model accounts for the nonresonant and resonant contributions to the signal and is summarized in Fig. 4.6. Equation (2) is used to account for the nonresonant contributions to the population transfer:

$$c_n(t) = \frac{\mu_{eg}}{h} \sum_p \frac{\varepsilon(\omega_p) \exp[i(\Delta_p)t - i\phi_p]}{\Delta_p}, \quad (4.5)$$

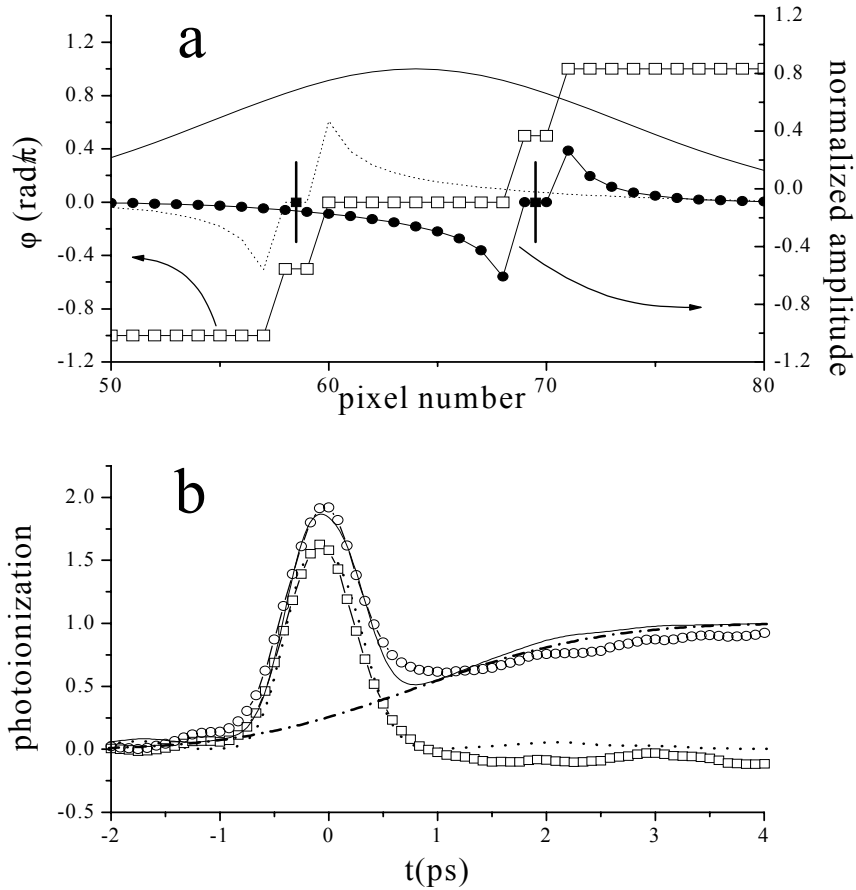


Fig. 4.6: Comparison of model results with experiment. Panel a: phase ( $\square$ ) and amplitude ( $\bullet$ ) [ $\epsilon(\omega_p)/\Delta_p$  from Eq. (4.5)] of the oscillations created by each pixel used to generate the nonresonant contribution to the model population transfer dynamics. Resonances are marked with vertical lines, and the electric field spectrum is given by the solid line. A second state (dashed line) is included for reference. Panel b: Comparison of model and experiment. The experimental nonresonant ( $\square$ ) and full population transfer traces ( $\circ$ ) are compared to the model nonresonant (dotted line) and full population transfer (solid line) traces. The model resonant contribution is given by the dot-dashed line.

where the summation is over all pixels ( $p$ ) of the SLM, with each pixel representing light of a specific frequency  $\omega_p$  and phase  $\phi_p$ . In essence, each pixel creates an oscillation with frequency  $\Delta_p$  and amplitude  $\varepsilon(\omega_p)/\Delta_p$ . Transform limited pulses with Gaussian spectral widths equal to experimental observations are assumed, giving  $\varepsilon(\omega_p)$ , and the quantum states are assumed to be symmetrically located under the spectral envelope. In Fig. 4.6a, the values of  $\varepsilon(\omega_p)/\Delta$  and  $\phi_p$  are plotted. The amplitude of the light at the two pixels around each resonance is assumed to be zero here, but it is accounted for in the resonant portion of the model. The signal is then computed as a convolution of the excited state population,  $|c_n(t)|^2$  with a 180 fs FWHM Gaussian probe pulse. The model population transfer dynamics fit very well with the experimental data, as shown in Fig. 4.6b. Using this model to quantify the influence of nonresonant frequencies, Eq. (4.2) shows that each state can be controlled up to 90% independently (*i.e.*  $I_{PTi}=0.90$ ).

The resonant contribution to the signal is modeled using Eq. (4.1). The electric field is assumed to be transform limited with a bandwidth for excitation equal to approximately  $10 \text{ cm}^{-1}$  FWHM, which corresponds to the light imaged onto two pixels. Each quantum state is assumed to be located at the central frequency of its respective narrow bandwidth region to best mimic experiment and to minimize computational artifacts related to the singularity at  $\Delta=0$ . This component of the modeled signal shows a slow, monotonic increase in the excited state population, just as one would expect from a several picosecond transform limited pulse. When the resonant and nonresonant components of the model are added together, they closely follow the experimental signal, as shown in Fig. 4.6b. A similar analysis was performed on the results using phase jump spectra with 0 radians relative phase, with similar outcomes, further supporting the

validity of this model. In future work, the effects of changing the energetic spacing between states will be used to experimentally verify the bandwidth considerations presented earlier.

We have shown the ability to independently implement the coherent control of both the population transfer coefficients and quantum interferences to two states in a superposition. Additionally, we have shown that the optimal pulse shape for transient population transfer in the weak field regime is characterized by nonresonant wavelengths that are shifted by  $\pi/2$  and  $-\pi/2$  radians relative to the resonant wavelengths. Using a simple model based upon the assumption that an ultrafast transition can be described by a collection of driven oscillators, we have quantified the degree to which the two states in the superposition can be independently controlled. This work should be instrumental for designing coherent control pulse schema and for understanding solutions found by various learning algorithms.